

# All-optical Fourier neural network using partially coherent light

Jianwei Qin<sup>1,†</sup>, Yanbing Liu<sup>2,†</sup>, Yan Liu<sup>1</sup>, Xun Liu<sup>3</sup>, Wei Li<sup>3,\*</sup>, Fangwei Ye<sup>1,§</sup>

<sup>1</sup>School of Physics and Astronomy, Shanghai Jiao Tong University,  
Shanghai 200240, China

<sup>2</sup>School of Electronic Engineering, Beijing University of Posts and Telecommunications,  
Beijing,100876,China

<sup>3</sup>Beijing Institute of Space Mechanics and Electricity,China Academy of Space Technology,  
Beijing,100094,China

\*E-mail: wei\_li\_bj@163.com

§E-mail: fangweiye@sjtu.edu.cn

**Optical neural networks present distinct advantages over traditional electrical counterparts, such as accelerated data processing and reduced energy consumption. While coherent light is conventionally employed in optical neural networks, our study proposes harnessing spatially incoherent light in all-optical Fourier neural networks. Contrary to numerical predictions of declining target recognition accuracy with increased incoherence, our experimental results demonstrate a surprising outcome: improved accuracy with incoherent light. We attribute this unexpected enhancement to spatially incoherent light's ability to alleviate experimental errors like diffraction rings, laser speckle, and edge effects. Our experiments introduced controllable spatial incoherence by passing monochromatic light through a spatial light modulator featuring a**

**dynamically changing random phase array. These findings underscore partially coherent light's potential to optimize optical neural networks, delivering dependable and efficient solutions for applications demanding consistent accuracy and robustness across diverse conditions.**

## 1 Introduction

All-optical neural networks (AONNs) utilize optical signals for data processing and computation, offering significant advantages over traditional electrical neural networks. The high propagation speed and transmission bandwidth of optical signals enable faster data processing, making AONNs particularly effective for the real-time processing of large datasets and neural network training. Additionally, photon transmission in AONNs is free from the electrical resistance and thermal dissipation found in electrical networks, resulting in lower energy consumption. AONNs typically perform spatial light computation through coherent diffraction effects. For example, diffraction-deep-neural networks (D2NN) (1–9) use the spatial adjustment of coherent light field phases to generate complex diffraction effects for optical computation. In image classification tasks, images input via coherent light sources pass through multiple phase masks, and the output light field intensity distribution is used for classification. D2NNs generally require several diffraction phase plates for image recognition. Another efficient architecture is the all-optical Fourier neural networks (AFNNs) (2, 10–14), which uses a spatial light modulator to adjust the phase spectrum of the input image light field at the Fourier plane of an optical 4F system. Classification is based on the light intensity distribution of the output field. The simpler and more adjustable optical path structure of the AFNNs, coupled with the coherence of the light field, ensures its high precision.

However, the reliance of AONNs on the output light intensity makes them highly sensitive to experimental errors in the distribution of the light field. Previous experimental studies on

AONNs have employed either fully coherent (1, 4–7, 9, 14, 14–25) or fully incoherent (26, 27, 27, 28) illumination methods. AONNs that are based on coherent light are highly susceptible to phase noise, such as diffraction noise from impurities in the optical system (29, 30) and laser speckle (31–33). Incoherent light sources, on the other hand, can mitigate the impacts of phase noise, but their accuracy were predicted in a few theoretical studies to fall below that of coherent light (34–36). Hence, the question arises: can an all-optical neural network be designed to reduce experimental errors stemming from the coherence of light while maintaining high accuracy?

It is commonly accepted that partially incoherent light favors the suppression of phase noise such as observed in optical holography and interferometry (37–42). In this work, we introduce the partially incoherent light into the optical neural networks, and, specifically, develop an AFNN based on partially coherent illumination. Consistent with previous theoretical studies (34–36), our numerical simulations indeed show a decrease in target recognition accuracy with increasing incoherence of the illumination light. Nevertheless, contrary to this numerical result, our experimental observations indicate enhanced accuracy in target recognition with the partially-coherent AFNN compared to its coherent counterparts. We attribute this enhanced performance to the ability of the incoherent light to be insensitive to the phase noise from environmental instability and experimental impurities that are unavoidably present in actual scenarios. Our experimental setup allows for adjustable degrees of spatial incoherence, enabling us to study the characteristics and performance of AFNN under varying degrees of incoherence. The incoherence is thus revealed as a novel degree of freedom for optical computation and networks, capable of improving the experimental accuracy and robustness of AONNs. This advancement holds promise for the integration and implementation of spatial light computing in realistic real-world conditions, where system tolerance unavoidably plays a crucial role (43, 44).

## 2 Generation and measurement of partially coherent light

Generating controllable partially-coherent light as an illumination source is essential for partially-coherent AFNN. For that purpose, we utilized a spatial light modulator (SLM) as a controllable dynamic scattering medium to generate partially-coherent light (45). In the experiment, a 532 nm wavelength laser source illuminates the SLM, which is loaded with time-varying random phase maps. These random phase patterns in SLM have a range of  $[(1 - \delta)\pi, (1 + \delta)\pi]$ , where  $\delta$  represents the modulation depth ( $0 < \delta < 1$ ). By rapidly switching the random phase maps on the SLM (at a 20 ms interval), the incident coherent light is converted into partially-coherent light. Adjusting the modulation depth  $\delta$  on the SLM allows control over the degree of incoherence, as illustrated in Fig. 1 (c).

In general, fully coherent light can be expressed as  $E = E_0 e^{i\phi}$ , where  $E_0$  represents the amplitude and  $\phi$  represents the phase. In contrast, for partially coherent or incoherent light, the phase  $\phi$  fluctuates rapidly and is described by its statistical properties:

$$W(r_1, r_2) = E_0(r_1)E_0(r_2)\langle e^{-i\phi(r_1)}e^{i\phi(r_2)} \rangle \quad (1)$$

where  $r_1$  and  $r_2$  are two spatial coordinates,  $\langle \dots \rangle$  represents the ensemble average. The degree of incoherence is defined as:

$$\mu_{light}(r_1, r_2) = 1 - \frac{W(r_1, r_2)}{\sqrt{W(r_1, r_1)W(r_2, r_2)}} = 1 - \langle e^{-i\phi(r_1)}e^{i\phi(r_2)} \rangle \quad (2)$$

For a given modulation depth  $\delta$ , the random phase  $\phi(r_1)$  follows the uniform probability distribution:  $P(\phi(r_i)) = \frac{1}{2\pi A_{light}}$ . Hence,

$$\langle e^{i\phi(r_i)} \rangle = \int_{-\infty}^{+\infty} e^{i\phi(r_i)} P(\phi(r_i)) d\phi(r_i) = \frac{\int_{(1-\delta)\pi}^{(1+\delta)\pi} e^{i\phi(r_i)} d\phi(r_i)}{2\pi\delta} = \text{sinc}(\delta) \quad (3)$$

Submission of Eq.3 into Eq.2 yields the degree of incoherence as following:

$$\mu_{light}(r_1, r_2) = \begin{cases} 0 & \text{if } r_1 = r_2 \\ 1 - \text{sinc}^2(\delta) & \text{if } r_1 \neq r_2 \end{cases} \quad (4)$$

Here, as expected, when  $\delta = 0$ , the light is fully coherent, and when  $\delta = 1$ , the light is fully incoherent. The blue line in Fig.1 (b) represents the simulated degree of incoherence at different  $\delta$ .

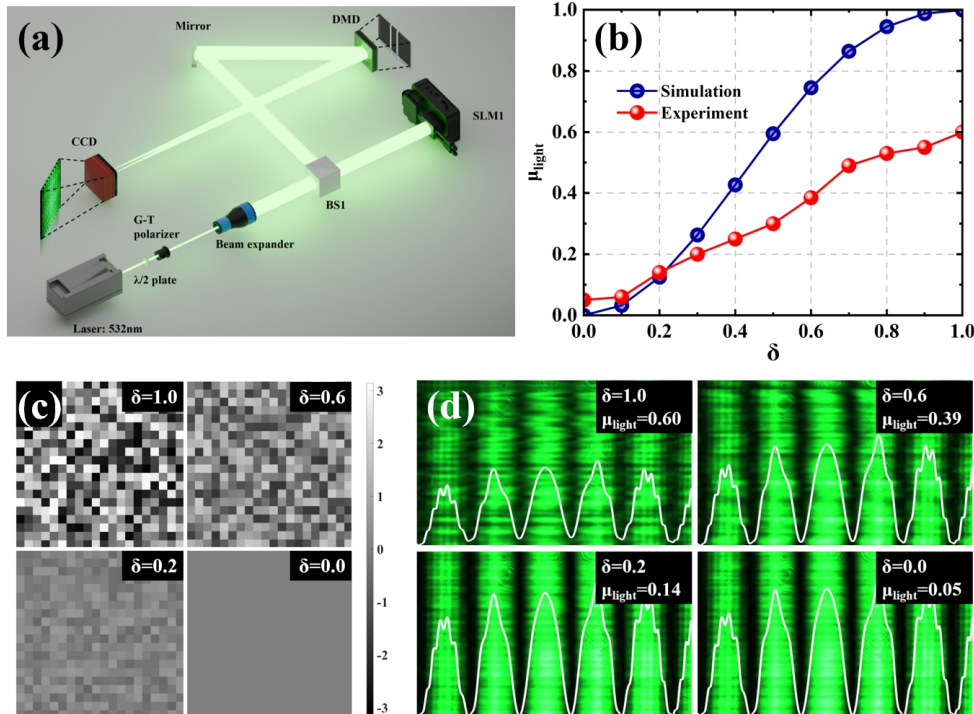


Figure 1: (a) Schematic diagram illustrating the experiment setup for generating incoherent light and measuring its degree of incoherence. Components: DMD-digital micromirror device loaded with a double-slit; SLM-spatial light modulator loaded with a random phase map; BS: beam splitter. (b) Calculated and experimentally measured degrees of incoherence as a function of random phase modulation depths  $\delta$ . The experimental curve is extracted from the double slit interference pattern (d) (cf. Eq. 5 of the text). (c) Random phase maps for four different modulation depths  $\delta$ . (d) Interference patterns of the incoherence light passing through the double-slit structure, for four different modulation depths of the random phase plate as shown in (c). The white curves in (d) represent the light intensity distribution along the horizontal axis.

Experimentally, as shown in Fig. 1 (a), we observe the interference fringes produced by different random modulation depths  $\delta$  on the SLM using a double-slit structure loaded on the

digital micromirror device (DMD). The degree of incoherence  $\mu_{light}$  is determined by measuring the contrast of the interference fringes:

$$\mu_{light} = 1 - \frac{I_{\max} - I_{\min}}{I_{\max} + I_{\min}} \quad (5)$$

where  $I_{\max}$  is the maximum light intensity and  $I_{\min}$  is the minimum light intensity. The interval time for switching the random phase patterns on the SLM is 10ms, and the CCD exposure time is one second. This setup ensures that 100 random phase patterns are loaded during each imaging process. Fig.1 (d) displays the interference patterns generated by different random phase modulation depths in the experiment. The degree of incoherence calculated from Eq.5 is shown as the red line in Fig.1 (b). Due to the influence of the SLM's fill factor and polarization effects, a portion of the coherent light incident on the SLM is directly reflected. This leads to a lower degree of incoherence in the experiment compared to the simulation.

It is worth mentioning that a recent study has proposed the use of partially incoherent light with narrow-band wavelength, namely, a *temporally* incoherent light, to reduce phase noise in optical computing chip and thus enhanced the performance of optical computing (46). This presents a stark contrast to our approach in achieving incoherence. The issue with temporally incoherence, or spectral broadening, is that it restricts the utilization of spectral resources, as the improvement in noise suppression comes at the expense of spectrum occupation. In contrast, our scheme relies on *spatially* incoherence, which functions perfectly even with a monochromatic light (as in the case of the present study), without requiring additional spectral resources. This offers the potential for more efficient wavelength-division multiplexing.

### 3 Architecture of partially-coherent all-optical Fourier neural network

Figure 2 (a) illustrates the architecture of a partially-coherent AFNN. This system begins with a SLM (SLM1) that rapidly switches a random phase pattern to convert coherent laser light into partially coherent light, serving as the illumination source. A DMD is then used to load the input images for classification. The partially coherent light field passes through a 4F system composed of two Fourier lenses. At the Fourier plane of this system, the second SLM modulates the spatial spectrum’s phase of the input light field with phase patterns trained for specific incoherence degrees. The resulting output light field is captured by a CCD, and classification is performed based on the light intensity in the classification region of the output light field.

To be more specific, the light field transmission in the partially coherent AFNN follows this process: Coherent light from the laser source, with amplitude  $E_0$ , passes through the first SLM, where it acquires a spatially random phase  $\phi_{x,y}^{rand}$ , resulting in  $E_1(x, y) = E_0 \cdot e^{\phi_{(x,y)}^{rand}}$ . By rapidly switching the random phase over time, the light is modulated into a partially coherent state. To simulate the propagating of this partially coherent light field, we treat it as the ensemble average of the propagation results of multiple coherent light fields, each subject to a different initial random phase modulation  $\phi_{x,y}^{rand}$ . The propagation of each individual light field  $E_1$  can be simulated using the Fresnel diffraction integral,

$$E_2(x, y) = E_1(x, y) \cdot t(x, y) \quad (6)$$

where  $t(x, y)$  represents the grayscale of the input image (in our case, handwritten numbers). The light field  $E_2$  enters into a 4F system, which consists of two Fourier lenses (each with focal length  $f$ ) and a SLM with a phase distribution  $\Psi(k_x, k_y)$  positioned at the Fourier plane of the first lens. The 4F system thus transforms  $E_2$  into  $E_3$  as follows,

$$E_3(x', y') = \mathcal{F}^{-1}[\mathcal{F}(E_2(x, y)) \cdot \Psi(k_x, k_y)] \quad (7)$$

where  $\mathcal{F}$  denotes the Fourier transform. We simulated the output light fields  $E_3(x', y')$  for 100 different random phase modulations of the initial coherent light  $E_1(x, y)$ , and by performing an ensemble average of these simulations, we obtained the output light intensity  $I_{out}$  for the partially coherent light, calculated as  $I_{out}(x, y) = \langle |E_3(x, y)|^2 \rangle$ .

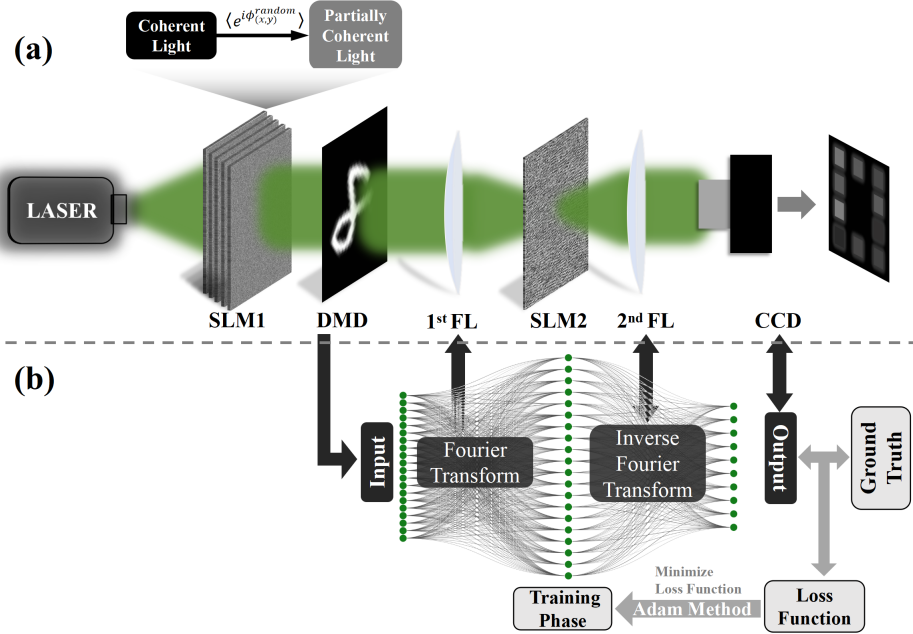


Figure 2: (a) Schematic diagram of partially-coherent AFNN architecture. FL: Fourier lens. (b) Flow chart of the training process. Note that the physical transformation of the 4F system is also used for back-propagation training of the AFNN.

We used the MNIST handwritten digit dataset for training in the image classification task. The training process for the partially coherent AFNN, as illustrated in Fig.2 (b), involves the following steps: (i) **Average pooling**. The output light field  $E_{out}(x, y)$  is divided into 10 classification spatial regions, each representing a digit from 0 to 9. The average light intensity within each region  $\Omega_i$  is recorded as an array,  $(I_0, I_1, \dots, I_9)$ , where  $I_i = \int_{\Omega_i} I_{out}(x, y) dx dy$ . These intensities are then converted into classification probabilities  $P_i$  using the softmax function,  $P_i = e^{I_i} / \sum_{i=0}^9 e^{I_i}$ . (ii) **Loss function**. During training, the classification probabilities are compared with the ground truth labels. The network's loss function is defined using cross-

entropy:  $L = -\sum_{i=0}^9 y_i \cdot \log(P_i)$  where  $y_i$  is a one-hot encoded vector representing the correct class (with  $y_i = 1$  for the correct class and  $y_i = 0$  otherwise). (iii ) **Backpropagation to train phase patterns.** The loss function is propagated back to the phase patterns on the second SLM using gradient descent, with the Adam optimizer computing the gradients and updating the training parameters. (iv) **Iterative training.** These steps are repeated iteratively, refining the phase patterns to improve classification accuracy until convergence is achieved. The final result is the optimal phase pattern  $\Psi(k_x, k_y)$ .

## 4 Experimental results

**Partial coherence enhanced AFNN.** Based on the architecture shown in Fig.2 (a), we constructed the experimental optical setup for the partially-coherent AFNN, as depicted in Fig.3 (a). A 532 nm laser served as the light source and it was converted into linearly polarized light using a half-wave plate and a Glan-Taylor polarizer, optimizing the modulation efficiency of the SLM. We used the Holoeye-LETO-80R SLM, which has a resolution of  $1920 \times 1200$ , a pixel size of  $8 \mu\text{m} \times 8 \mu\text{m}$ , a fill factor of 95%, and a phase modulation range of 0 to  $2\pi$  (corresponding to grayscale values of 0 to 255). The first SLM, responsible for converting coherent light into partially coherent light, had an active area of  $15.4 \text{ mm} \times 9.6 \text{ mm}$ , exceeding the beam size (approximately 8.3 mm radius) to ensure full beam modulation. However, the minimum unit size for random phase modulation,  $8 \mu\text{m} \times 8 \mu\text{m}$ , was larger than the ideal infinitesimal size, resulting in a lower degree of incoherence in the experiment compared to simulations. The DMD used to load input images was a Texas Instruments DLPC900, with a resolution of  $1920 \times 1080$  and a pixel size of  $7.56 \mu\text{m} \times 7.56 \mu\text{m}$ . In the 4F system used for image classification, both Fourier lenses had a focal length of 15 mm, and the second SLM loaded phase maps trained for specific degree of incoherence. The CCD used to capture output images had a maximum light intensity threshold of  $13.8 \text{ mW/m}^2$ , truncating any intensity beyond this limit. For a given

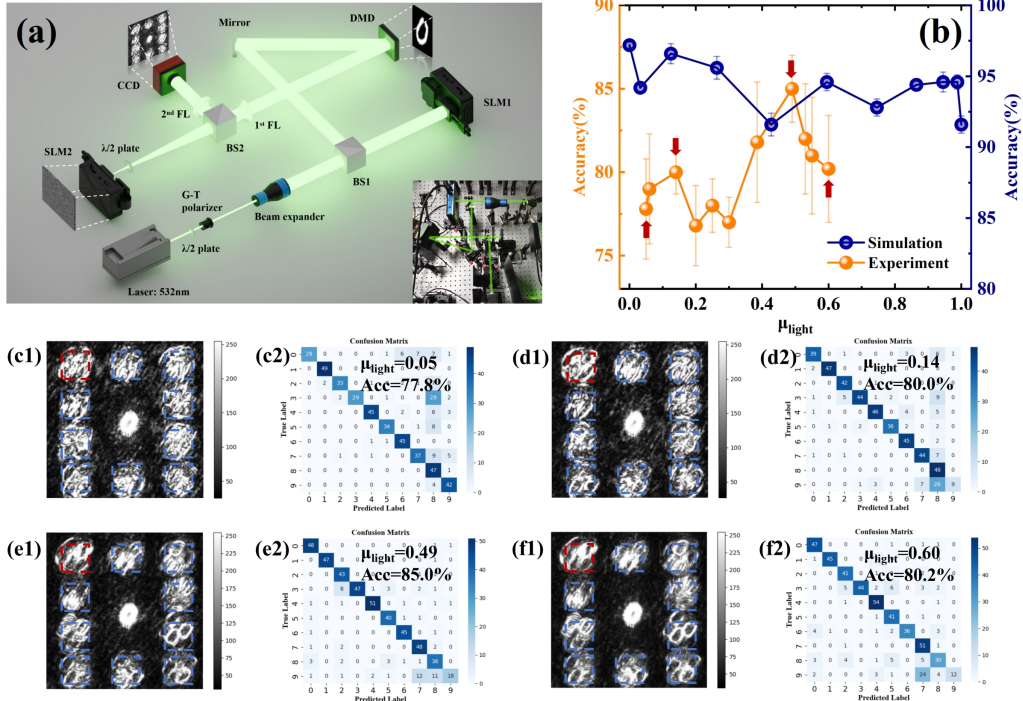


Figure 3: (a) Experimental schematic of the partially-coherent AFNN with an inset showing a photo of the experimental setup. (b) Simulation and experimental classification accuracy of the partially-coherent AFNN on the MNIST dataset under varying degrees of incoherence, both averaged 10 independent realizations in the phase map loaded onto SLM2. (c1-f1) Output light fields captured by the CCD at incoherence degrees of 0.05, 0.14, 0.49, and 0.60, respectively. The classification is based on the mean light intensity within boxed regions, and the region of maximum light intensity determines the classification result (the red box for the specific test shown). (c2-f2) Confusion matrices depicting the inference results of the partially-coherent AFNN at incoherence degrees of 0.05, 0.14, 0.49, and 0.60, respectively.

degree of incoherence, an optimal phase map is obtained through the aforementioned training process and loaded on SLM2. We used 500 test images from the MNIST dataset to verify the classification accuracy of the partially-coherent AFNN under different incoherence degrees, both in simulations and experiments.

As shown by the blue curve in Fig. 3(b), our simulations indicate that increasing incoherence typically leads to a decrease in network accuracy, with 97.2% accuracy at perfect coherence ( $\mu_{light} = 0$ ) and 91.6% accuracy at full incoherence ( $\mu_{light} = 1.0$ ). However, in the experiment,

coherent light introduces detrimental effects such as diffraction rings, laser speckle, and edge effects, resulting in a lower accuracy of 77.8% under an almost fully coherent conditions (Fig.3, c1 and c2). Remarkably, by introducing partial incoherence, we observed an improvement in experimental accuracy. At a moderate incoherence degree of 0.14, the experimental accuracy increased to 80.0% (Fig. 3, d1 and d2), and the highest accuracy of 85.0% was achieved at an incoherence degree of 0.49 (Fig. 3, e1 and e2). This counterintuitive result-where accuracy improves as incoherence increases-demonstrates the effectiveness of partially coherent light in mitigating the adverse effects associated with coherent light. However it should be noted that, further increasing the level of incoherence beyond the optimal point led to a decrease in accuracy (Fig. 3, f1 and f2). The experimental trend of classification accuracy as a function of incoherence is summarized by the orange curve in Fig. 3 (b).

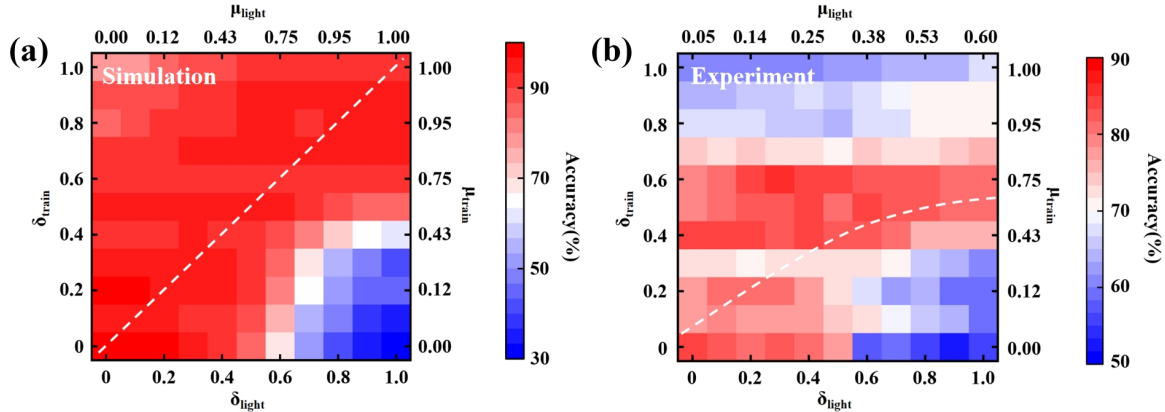


Figure 4: (a) The simulated inference accuracy of the partially-coherent AFNN, assessed with a phase map trained for incoherence degree of  $\mu_{train}$  (random phases modulation depth  $\delta_{train}$ ), but illuminated by partially coherent light with incoherence degree of  $\mu_{light}$  (random phase modulation depth  $\delta_{light}$ ). (b) The same as (a), but for the experimental measured inference accuracy. The white dashed lines represent points where  $\mu_{light} = \mu_{train}$ , and the corresponding accuracy along this line is shown in Fig. 3 (b).

**Incoherence tolerance in partially coherent AFNNs.** Now, suppose the phase map, which has been trained under illumination by partially coherent light with a degree of incoherence  $\mu$

(denoted as  $\mu_{train}$  in following), is loaded onto SLM2. This trained AFNN is expected to perform optimally when the illumination light has the same degree of incoherence as in the training process. However, in practical applications, the degree of incoherence of the actual illumination light, denoted as  $\mu_{light}$ , may differ from  $\mu_{train}$ . This raises the question: how does the performance of the partially coherent AFNN, trained with the light of incoherence  $\mu_{train}$ , change when in actual applications the incoherence of the illumination light,  $\mu_{light}$ , differs?

To answer this question, we study the classification accuracy of systems trained with incoherence  $\mu_{train}$ , but illuminated with light of incoherence  $\mu_{light}$  that may occur in real applications. The results are shown in Fig.4, with simulations in (a) and experimental data in (b), both plotted on a 2D plane with axes  $\mu_{light}$  and  $\mu_{train}$  (or equivalently  $\delta_{light}$  and  $\delta_{train}$ , recalling that the modulation depth of the phase determines the degree of incoherence). As expected, the highest classification accuracy is generally achieved when the incoherence of the illumination light matches the training condition ( $\mu_{light} = \mu_{train}$ ), as indicated by the white dashed line in Fig.4. Also as expected, when the incoherence of the illumination light,  $\mu_{light}$ , deviates from that of the trained model,  $\mu_{train}$ —whether  $\mu_{light} > \mu_{train}$  or  $\mu_{light} < \mu_{train}$ —the accuracy decreases, but interestingly in notably different ways. When  $\mu_{light} > \mu_{train}$ , meaning the system is illuminated by a more incoherent light than it was trained for, the classification accuracy drops sharply with increasing incoherence mismatch. For instance, when the AFNN is trained with fully coherent light ( $\mu_{train} = 0$ ), the simulation results show that the accuracy is 97.2% when  $\mu_{light} = 0$ , but drops drastically to 32.4% when  $\mu_{light} = 1.0$ . The experimental results show that the accuracy drops from 77.8% when  $\mu_{light} = 0.05$  to 55.9% when  $\mu_{light} = 0.60$ . In contrast, when  $\mu_{light} < \mu_{train}$ , meaning the system is illuminated by a less incoherent light than it was trained with, the accuracy remains relatively high despite the incoherence mismatch. For example, for AFNNs trained with fully incoherent light ( $\mu_{train} = 1.0$ ), the simulation results show that, while the accuracy is 91.6% when  $\mu_{light} = 1.0$ , even when a fully coherent light is

used for illumination ( $\mu_{light} = 0$ ), the accuracy remains as high as 79.2%. Experimentally, for the AFNN trained with  $\mu_{train} = 0.6$ , the accuracy is 80.2% when  $\mu_{light} = 0.6$  and 79.5% when  $\mu_{light} = 0$ .

The ability of an AFNN trained with high incoherence to maintain high accuracy under lower incoherence illumination, while an AFNN trained with low incoherence struggles under highly incoherent illumination, is connected to the phase modulation of the spatial spectrum generated by the input image at the Fourier plane. Typically, the spatial spectrum expands as the incoherence of the illumination light increases. Using Fig. 5 as an illustration for the same input image (a digit “zero”), when lit with highly coherent light ( $\mu_{light} = 0.05$ ), the spatial spectrum is mainly concentrated near the center of the Fourier plane (Fig. 5, a2), occupying the third smallest square. In contrast, under a light with  $\mu_{light} = 0.6$ , the spectrum widens significantly, even reaching the largest square (Fig. 5, a4). Therefore, in practical applications, when AFNNs are trained with a certain incoherence light with  $\mu_{train}$ , using a higher incoherent illumination source ( $\mu_{light} > \mu_{train}$ ) leads to a broader coverage of the phase plate at the Fourier plane compared to the trained one, thus resulting in a significant drop in classification accuracy. Conversely, with lower incoherent light ( $\mu_{light} < \mu_{train}$ ), the Fourier spectrum occupies a smaller portion of the already-trained phase plate, thus maintaining relatively high accuracy (though lower than with matched incoherent illumination). This rationale is further supported by Fig. 5(b), where the performance of AFNNs under different incoherent light illuminations is evaluated with varying phase plate sizes (specifically, SLM2 in our setup). The results show that as the size of the phase plate increases, the network accuracy improves for all illumination conditions but saturates at different plate sizes. For instance, with light at  $\mu_{light} = 0.05$  (blue line in Fig. 5(b)), accuracy saturates at an SLM size of  $0.8 \times 0.8\text{mm}^2$ , as this size is already large enough to modulate all spectral components at the Fourier plane (corresponding to the third smallest box in Fig. 5, a2). In contrast, for  $\mu_{light} = 0.30$ , accuracy convergence requires

SLM sizes larger than  $1.6 \times 1.6\text{mm}^2$  (forth smallest box in Fig. 5, a3). Further, for  $\mu_{\text{light}} = 0.60$ , accuracy stabilizes for SLM sizes exceeding  $4.8 \times 4.8\text{mm}^2$  (the biggest box in Fig. 5, a4). This highlights that the classification accuracy continues to rise as the SLM size increases to handle higher Fourier components, plateauing once surpassing the spectral range, indicating that further size increases do not impact accuracy.

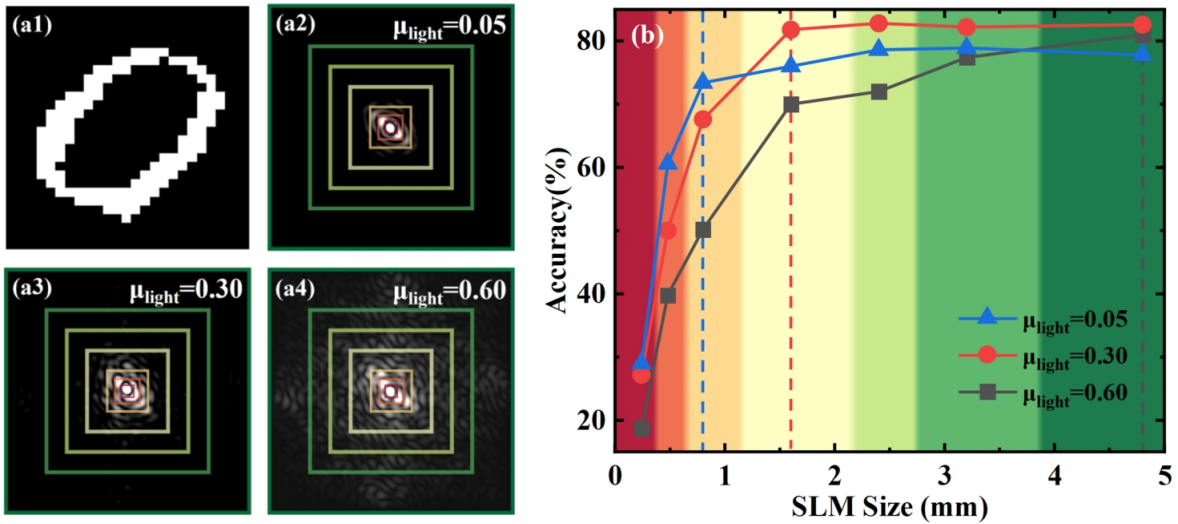


Figure 5: (a1) An image of the digit '0' from the MNIST dataset. (a2-a4) Experimentally measured intensity spectra of the image in (a1) when illuminated with partially coherent light, with degree of incoherence set to 0.05, 0.30, and 0.60, respectively. (b) Inference accuracy of the AFNN measured as a function of SLM size, corresponding to the seven square regions indicated in (a2-a4). The dashed vertical lines in (b) indicate the SLM sizes at which the accuracy converges.

## 5 Conclusion

In conclusion, we have developed an all-optical Fourier neural network (AFNN) utilizing partially coherent light, significantly improving experimental accuracy compared to fully coherent systems. By adjusting the degree of incoherence in the illumination source, we address coherence-induced experimental errors, offering a new degree of freedom in optical computa-

tion. Our experiments with the MNIST dataset show that partially-coherent AFNN achieves higher accuracy at optimal incoherence degrees, mitigating the detrimental effects of coherent light such as diffraction rings and laser speckles.

Looking ahead, the capability to fine-tune the degree of spatial incoherence opens up new possibilities to enhance the performance and accuracy of optical neural networks across diverse environments. This advancement not only improves the potential of AONNs but also opens doors to a wider range of applications, including real-time image classification, biomedical imaging, and optical signal processing, where accuracy and robustness are paramount. Furthermore, our proposed architecture has the experimental flexibility to straightforwardly include optically nonlinear active functions (e.g., implemented with optical nonlinear crystals), which is expected to play a vital role in handling more challenging tasks. Finally, our proposed spatially incoherent AONN, in combination with temporally incoherent modulation (46), is promising to enable operation under spatially and temporally incoherent (i.e., "white light") conditions, such as natural light. Optical neural networks effectively operating under natural light scenarios hold substantial promise for practical and robust applications, and our results lay a promising foundation for realizing this vision.

## Author contributions

F.Y. and W.L. initiated and supervised the project. J.Q. designed the research and methodology. J.Q. and Y.L. carried out the simulations and data processing. J.Q. conducted the experiments. Y.L. and J.Q. developed the experimental system. J.Q, F.Y., Y.L, Y.L, X.L., and W.L. analyzed the results. F.Y. and J.Q. prepared the manuscript with contributions from all authors. All authors participated in discussions regarding the research.

## Data availability

All the data and methods required to assess the conclusions of this study are provided in the main text. Additional data can be requested from the corresponding author. The codes used in this study rely on standard libraries and scripts, which are publicly accessible in PyTorch.

## Acknowledgements

This work was supported in part by the National Natural Science Foundation of China under grant U23B2011 and 62220106008.

## Conflict of interest

No author has reported any competing interests.

## References and Notes

1. X. Lin, *et al.*, All-optical machine learning using diffractive deep neural networks. *Science* **361** (6406), 1004–1008 (2018).
2. T. Yan, *et al.*, Fourier-space diffractive deep neural network. *Physical Review Letters* **123** (2), 023901 (2019).
3. C. Liu, *et al.*, A programmable diffractive deep neural network based on a digital-coding metasurface array. *Nature Electronics* **5** (2), 113–122 (2022).
4. J. Li, *et al.*, Spectrally encoded single-pixel machine vision using diffractive networks. *Science Advances* **7** (13), eabd7690 (2021).
5. T. Zhou, *et al.*, Large-scale neuromorphic optoelectronic computing with a reconfigurable diffractive processing unit. *Nature Photonics* **15** (5), 367–373 (2021).

6. Y. Li, J. Li, A. Ozcan, Nonlinear encoding in diffractive information processing using linear optical materials. *Light: Science & Applications* **13** (1), 173 (2024).
7. Ç. İşil, *et al.*, All-optical image denoising using a diffractive visual processor. *Light: Science & Applications* **13** (1), 43 (2024).
8. Y. Luo, *et al.*, Design of task-specific optical systems using broadband diffractive neural networks. *Light: Science & Applications* **8** (1), 112 (2019).
9. M. S. S. Rahman, J. Li, D. Mengu, Y. Rivenson, A. Ozcan, Ensemble learning of diffractive optical networks. *Light: Science & Applications* **10** (1), 14 (2021).
10. L. Bernstein, *et al.*, Single-shot optical neural network. *Science Advances* **9** (25), eadg7904 (2023).
11. Y. Liu, *et al.*, Optical Fourier convolutional neural network with high efficiency in image classification. *Optics Express* **32** (13), 23575–23583 (2024).
12. M. Miscuglio, *et al.*, Massively parallel amplitude-only Fourier neural network. *Optica* **7** (12), 1812–1819 (2020).
13. Y. Liu, *et al.*, Towards constructing a DOE-based practical optical neural system for ship recognition in remote sensing images. *Signal Processing* **221**, 109488 (2024).
14. Y. Zuo, *et al.*, All-optical neural network with nonlinear activation functions. *Optica* **6** (9), 1132–1137 (2019).
15. J. Spall, X. Guo, A. I. Lvovsky, Hybrid training of optical neural networks. *Optica* **9** (7), 803–811 (2022).

16. T. Zhou, *et al.*, In situ optical backpropagation training of diffractive optical neural networks. *Photonics Research* **8** (6), 940–953 (2020).
17. Z. Chen, *et al.*, Deep learning with coherent VCSEL neural networks. *Nature Photonics* **17** (8), 723–730 (2023).
18. H. Zhang, *et al.*, An optical neural chip for implementing complex-valued neural network. *Nature Communications* **12** (1), 457 (2021).
19. S. Xu, *et al.*, Optical coherent dot-product chip for sophisticated deep learning regression. *Light: Science & Applications* **10** (1), 221 (2021).
20. A. Montes McNeil, Y. Li, A. Zhang, M. Moebius, Y. Liu, Fundamentals and recent developments of free-space optical neural networks. *Journal of Applied Physics* **136** (3) (2024).
21. Y. Zhang, *et al.*, Memory-less scattering imaging with ultrafast convolutional optical neural networks. *Science Advances* **10** (24), eadn2205 (2024).
22. J. Cheng, *et al.*, Multimodal deep learning using on-chip diffractive optics with in situ training capability. *Nature Communications* **15** (1), 6189 (2024).
23. Y. Shen, *et al.*, Deep learning with coherent nanophotonic circuits. *Nature Photonics* **11** (7), 441–446 (2017).
24. O. Kulce, D. Mengu, Y. Rivenson, A. Ozcan, All-optical synthesis of an arbitrary linear transformation using diffractive surfaces. *Light: Science & Applications* **10** (1), 196 (2021).
25. X. Fang, *et al.*, Orbital angular momentum-mediated machine learning for high-accuracy mode-feature encoding. *Light: Science & Applications* **13** (1), 49 (2024).

26. T. Wang, *et al.*, Image sensing with multilayer nonlinear optical neural networks. *Nature Photonics* **17** (5), 408–415 (2023).
27. M. S. S. Rahman, X. Yang, J. Li, B. Bai, A. Ozcan, Universal linear intensity transformations using spatially incoherent diffractive processors. *Light: Science & Applications* **12** (1), 195 (2023).
28. Y. Fei, X. Sui, G. Gu, Q. Chen, Zero-power optical convolutional neural network using incoherent light. *Optics and Lasers in Engineering* **162**, 107410 (2023).
29. A. V. Martin, *et al.*, Noise-robust coherent diffractive imaging with a single diffraction pattern. *Optics Express* **20** (15), 16650–16661 (2012).
30. P. Godard, M. Allain, V. Chamard, J. Rodenburg, Noise models for low counting rate coherent diffraction imaging. *Optics Express* **20** (23), 25914–25934 (2012).
31. S. E. Skipetrov, *et al.*, Noise in laser speckle correlation and imaging techniques. *Optics Express* **18** (14), 14519–14534 (2010).
32. A. C. Völker, P. Zakharov, B. Weber, F. Buck, F. Scheffold, Laser speckle imaging with an active noise reduction scheme. *Optics Express* **13** (24), 9782–9787 (2005).
33. J. C. Dainty, *Laser speckle and related phenomena*, vol. 9 (Springer science & business Media) (2013).
34. M. J. Filipovich, A. Malyshev, A. Lvovsky, Role of spatial coherence in diffractive optical neural networks. *Optics Express* **32** (13), 22986–22997 (2024).
35. M. J. Filipovich, A. Malyshev, A. Lvovsky, Diffractive optical neural networks with arbitrary spatial coherence, in *Machine Learning with New Compute Paradigms* (2023).

36. M. Kleiner, L. Michaeli, T. Michaeli, Coherence Awareness in Diffractive Neural Networks, in *CLEO: Fundamental Science* (Optica Publishing Group) (2024), pp. FW4Q–5.
37. Y. Peng, S. Choi, J. Kim, G. Wetzstein, Speckle-free holography with partially coherent light sources and camera-in-the-loop calibration. *Science Advances* **7** (46), eabg5040 (2021).
38. R. H. Brown, R. Twiss, Interferometry of the intensity fluctuations in light. II. An experimental test of the theory for partially coherent light. *Proceedings of the Royal Society of London. Series A. Mathematical and Physical Sciences* **243** (1234), 291–319 (1958).
39. J. Clark, X. Huang, R. Harder, I. Robinson, High-resolution three-dimensional partially coherent diffraction imaging. *Nature Communications* **3** (1), 993 (2012).
40. C. Bourassin-Bouchet, M.-E. Couplie, Partially coherent ultrafast spectrography. *Nature Communications* **6** (1), 6465 (2015).
41. Z. Shi, *et al.*, Super-resolution orbital angular momentum holography. *Nature Communications* **14** (1), 1869 (2023).
42. Y. Tang, *et al.*, Active and low-cost hyperspectral imaging for the spectral analysis of a low-light environment. *Sensors* **23** (3), 1437 (2023).
43. D. Mengu, *et al.*, Misalignment resilient diffractive optical networks. *Nanophotonics* **9** (13), 4207–4219 (2020).
44. D. Mengu, Y. Rivenson, A. Ozcan, Scale-, shift-, and rotation-invariant diffractive optical networks. *ACS photonics* **8** (1), 324–334 (2020).
45. Y. Cai, Y. Chen, J. Yu, X. Liu, L. Liu, Generation of partially coherent beams. *Progress in Optics* **62**, 157–223 (2017).

46. B. Dong, *et al.*, Partial coherence enhances parallelized photonic computing. *Nature* **632** (8023), 55–62 (2024).